Global two-fluid turbulence simulations of L-H transitions and edge localized mode dynamics in the COMPASS-D tokamak

A. Thyagaraja, M. Valovič, and P. J. Knight
EURATOM/CCFE Fusion Association, Culham Science Centre, Abingdon, OX14 3DB, United Kingdom

(Received 28 December 2009; accepted 12 March 2010; published online 26 April 2010)

It is shown that the transition from L-mode to H-mode regimes in tokamaks can be reproduced using a two-fluid, fully electromagnetic, plasma model when a suitable particle sink is added at the edge. Such a model is implemented in the CUTIE code [A. Thyagaraja *et al.*, Eur. J. Mech. B/Fluids **23**, 475 (2004)] and is illustrated on plasma parameters that mimic those in the COMPASS-D tokamak with electron cyclotron resonance heating [Fielding *et al.*, Plasma Phys. Contr. Fusion **42**, A191 (2000)]. In particular, it is shown that holding the heating power, current, and magnetic field constant and increasing the fuelling rate to raise the plasma density leads spontaneously to the formation of an edge transport barrier (ETB) which occurs going from low to higher density experimentally. In the following quiescent period in which the stored energy of the plasma rises linearly with time, a dynamical transition occurs in the simulation with the appearance of features resembling strong edge localized modes. The simulation qualitatively reproduces many features observed in the experiment. Its relative robustness suggests that some, at least of the observed characteristics of ETBs and L-H transitions, can be captured in the global electromagnetic turbulence model. [doi:10.1063/1.3381074]

I. INTRODUCTION

Understanding edge transport barriers (ETBs) associated with L- to H-mode transitions in tokamaks, particularly in electron-heated conditions, remains an important and scientifically interesting issue for ITER (see Aymar *et al.*[1]). In recent years there have been many studies, both experimental and theoretical (for the latter, see, for example, works by Rogers *et al.*,[2] Kleva and Guzdar,[3] Carreras *et al.*,[4] Itoh *et al.*,[5,6] Thyagaraja *et al.*,[7] and the very recent, remarkable simulations of Huysmans *et al.*[8]) of the problems associated with ETBs. In spite of this extensive research, many serious questions remain to be answered in the actual characterization of the phenomena and the conditions pertaining to stability and transport associated with edge localized modes (ELMs) which often accompany such transport barriers. An excellent recent review by Connor, Kirk, and Wilson[9] should be consulted about the current understanding of ELM phenomena. In fusion devices like ITER, it is expected that the electrons will be predominantly heated by the fusion alphas. There are important requirements on the electron density required for optimal operation. It is therefore essential to understand experimentally and theoretically how L-H transitions evolve and the dynamical behavior to be expected from ELMs when the input power is kept relatively constant, but the line-averaged density $\bar{n}_e$ is a control parameter (perhaps varied using pellets or gas puff).

The aim of this paper is to demonstrate that the L-H transition can be reproduced using a two-fluid, fully electromagnetic, global turbulence model. An important element of the model is the introduction of a particle source in the confined region and a particle sink at the edge. In addition, profile-turbulence interactions should be allowed to develop. The paper is organized as follows. In Sec. II we describe the H-mode plasma in COMPASS-D tokamak which motivated our numerical simulations. Section III describes the CUTIE code used in this study. In Sec. IV we present the results of the simulations and in Sec. V we discuss our findings and how they relate to earlier work and finally present our conclusions.

II. EXPERIMENTAL CONDITIONS SIMULATED

In this section we describe the COMPASS-D plasmas which have been used to motivate the present simulation studies employing the CUTIE turbulent transport code (described in the next section). The COMPASS-D tokamak operated at Culham Science Centre was a relatively small device (see Refs. 10–15) equipped with shaping coils allowing divertor operation. Electron-cyclotron resonance heating (ECRH) was employed as an auxiliary power source. The H-mode in COMPASS-D was accessed using both Ohmic and ECRH heatings with a single null divertor and a favorable direction of ion grad-B drift (i.e., toward the X-point). This device is now at the Institute of Plasma Physics, Prague in the Czech Republic as a research tokamak.

From the beginning of COMPASS-D operation it was clear that the L-H threshold was not simply governed by the conventional power threshold law $P > nB$ but that some minimum plasma density is required for L-H transition, see Ref. 1. For example, at the launched power $P_{\mathrm{ech}} \simeq 0.5$ MW and magnetic field ($B_{\mathrm{tor}} = 2.07$ T) the ELMy H-modes appeared only for line-average densities above 3.6×10^{19} m^{-3}.[13] The role of edge plasma density in L-H transition was also confirmed by observations for Ohmic plasmas where L-H transition was typically induced by strong puffing followed by sharp gas-turned off. Inboard gas puffing[14,15] and pellet injection[16,17] also were found to im-

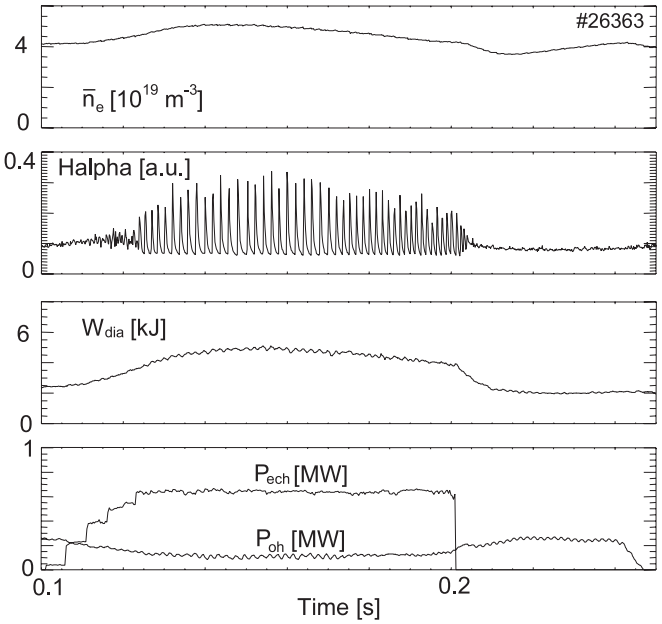

FIG. 1. COMPASS-D Shot No. 26363: $\bar{n}_e$ is the line-averaged density, H_α is the Balmer line emission, W_{dia} is the plasma energy content measured by diamagnetic loop, P_{oh} is the Ohmic heating power, and P_{ecrh} is the ECH heating power. Plasma current is I_p=242 kA and the toroidal magnetic field at the magnetic axis is B_T=2.07 T.

prove the transition to H-mode indicating the role of plasma density in L-H transition.

As a case study for CUTIE simulation we have chosen a typical stationary ELMy H-mode with on-axis ECRH heating. Time traces of such a discharge are shown in Fig. 1. These plasmas were originally used for energy confinement studies and described in greater detail in Ref. 9. In this ECRH dominated ELMy H-mode, the auxiliary heating was applied at the fundamental resonance. In this regime the waves (at 60 GHz frequency) were launched from up to five high field side antennae with X-mode polarization into the plasma with toroidal magnetic field on geometric axis of B_{tor}=2.07 T. In order to ensure absorption of wave energy at the fundamental resonance layer, the waves were chosen to propagate obliquely relative to the major radius (33° at launch position). Launching angles were balanced as far as possible so that no significant current drive was expected. Single null, diverted Deuterium plasmas (minor radius a=0.17 m, major radius R=0.56 m, elongation=1.7, and triangularity=0.4) were used in this experiment. It was estimated that the ECH power actually absorbed in the plasma is 340 kW. The transition from L-mode to ELMy H-mode was typically gradual through a period of small, high frequency ELMs. In order to achieve a regime with well-separated ELMs, plasma shape with increased triangularity was found necessary although no systematic comparisons were made. These ELMy H-regimes could persist for the whole duration of the heating pulse as illustrated in Fig. 1. In these experiments the maximum plasma current was 242 kA. With decreasing plasma current, the ELM frequency decreased and at I_p=150 kA ELM-free H-mode was observed. At low plasma current, L-H transitions become sharp, no longer with concurrent high frequency ELMs.

III. DESCRIPTION OF CUTIE

The purpose of the present paper is to describe extensive numerical studies made with the CUTIE code. In order to make this paper self-contained the principal equations and features of the CUTIE model are presented in the Appendix. Detailed descriptions of the two-fluid plasma model used in the code, numerical schemes employed, and many previous comparisons with experiments can be found in Refs. 18–21. In this work we investigate the hypothesis that L-H transition phenomena observed in the COMPASS-D experiments can be qualitatively understood in terms of a two-fluid electromagnetic model implemented in CUTIE. We stress that no attempt is made to reproduce the experimental results with the simulations in quantitative detail. The latter are motivated by the experimental conditions summarized in Sec. I, but the aim of the study is to explore the dynamical capabilities of the electromagnetic turbulence model embodied in the CUTIE code and to gauge the extent to which it is able to account for observed phenomena.

A. Confinement region

The key ideas of the quasineutral two-fluid model, implemented in CUTIE are outlined. Details are available in the references cited. The plasma is taken to consist of electrons and a single species of ions which is deuterium in COMPASS-D. We assume, $n_e \simeq n_i = n$ and $\mathbf{j} = c/4\pi \nabla \times \mathbf{B}$ ("quasineutrality"). Impurities are not explicitly treated. A Z_{eff} radial profile (unity at the magnetic axis and rising monotonically with r/a) is assumed and kept fixed throughout the simulations. This influences the resistivity of the plasma (and loop voltage) but is not taken into account otherwise in the simulation (for example, via possible radiative losses in the energy balance). Each species is assumed to be locally Maxwellian but $T_i \neq T_e$ in general. The model does not account for kinetic/velocity space (linear or nonlinear) effects. On the other hand, many drift effects usually neglected in ideal and resistive magnetohydrodynamics (MHD) are included. We employ a "generalized Ohm's law"[22] which incorporates the Hall effect and electron diamagnetism but neglects electron inertia. It is technically possible to include the latter effect but for the fact that at such high spatial resolutions, the calculational times would become prohibitively long, not to mention the fact that the fluid model is inadequate to represent subion gyroradius physics.

A large aspect ratio $R/a \gg 1$ tokamak ordering, $B_{\mathrm{pol}} \ll B_{\mathrm{tor}}$, $\beta \ll 1$, $k_\parallel \ll k_\perp$ is used in the CUTIE model which includes field-line bending and curvature but neglects some stabilizing effects (due to Shafranov shifts). Neoclassical theory[22] is assumed to provide a minimum level of transport. Particle and energy source profiles (except Ohmic heating) are not calculated in detail, but simply prescribed in accordance with transport codes. The prescriptions used in the present simulations will be discussed in the next section. Conservation equations for particles, energy and momentum, and Maxwell's equations are solved (these are given in the Appendix; see also, Refs. 19 and 20) to obtain the electron number density (n), species temperatures ($T_{e,i}$), ion fluid ve-

locity ($\mathbf{v}$), electrostatic potential (Φ), and the parallel vector potential (equivalent to the poloidal flux function) (Ψ).

In the code, mesoscales {time-scales between the Alfvén time $[\tau_A = qR_0/V_A;\ V_A = B_{\rm tor}/(4\pi m_i n_e)^{1/2}]$ and the resistive time $(\tau_{\rm res} = 4\pi a^2/c^2\eta_{\rm nc})$, and length-scales $L_{\rm meso}$ satisfying $\rho_s < L_{\rm meso} < a$ are modeled, where $\Omega_{ci} = eB_{\rm tor}/m_i c$ and $\Omega_{ci}^2\rho_s^2 = C_s^2 = (T_i + T_e)/m_i$. The flux surface averaged quantities and the turbulence are coevolved in a self-consistent manner (resolving shear Alfvénic modes). In the simulations presented we have used 101 radial grid points, 64 poloidal, and 16 toroidal Fourier modes. The time-step used in the simulations was $\Delta t = 5 \times 10^{-8}$ s; for comparison, the shear Alfvén time $qR/V_A \geq 5 \times 10^{-7}$ s. The radial grid resolution is adequate to just resolve the ion gyroradius $\simeq 0.5$ cm. Limited grid convergence studies show that lowering the time-steps and increasing the poloidal resolution does not significantly affect any of the results obtained. Systematic resolution studies are very difficult as the computation times for the presented long duration simulations would become prohibitively time-consuming with higher resolution. The code is implemented on a unix work-station (2 GHz) operating in serial mode. A typical 2 ms real time COMPASS-D simulation run takes about 48 h. The presented work is a composite of many such runs continued in sequence.

The CUTIE dynamics includes the following fluidlike modes: linear and nonlinear shear Alfvén waves, slow magnetoacoustic modes, drift-tearing modes, ballooning (ideal and viscoresistive branches) modes; the fluid branch of the ion temperature gradient (ITG)-driven instability is also included. Profile gradients interact nonlinearly with the turbulence. This profile-turbulence interaction involves characteristic "cross-talk" via the equations of motion between the profile gradients on the one hand which tend to drive the turbulence (both linearly and nonlinearly, in general), while the latter in its turn tends to reduce the driving gradients via enhanced transport in the presence of fixed external sources. The poloidal magnetic field (consequently the safety factor $q = rB_{\rm tor}/RB_\theta$) evolves in time and space according to the induction equation

$$\frac{\partial \langle B_\theta \rangle}{\partial t} = c\frac{\partial \langle E_\zeta \rangle}{\partial r}, \tag{1}$$

where $\langle\ \rangle$ denotes averaging over a flux surface and $\langle E_\zeta \rangle = \eta_{\rm nc}(\langle j_\zeta \rangle - j_{\rm bs} - j_{\rm dyn})$. The "dynamo current" $j_{\rm dyn} = \langle \hat{\mathbf{e}}_\zeta \cdot (\delta \mathbf{v} \times \delta \mathbf{B}) \rangle / c\eta_{\rm nc}$ is driven by the correlations between fluctuations of $\mathbf{v}, \mathbf{B}$. In the foregoing equation, we use standard neoclassical expressions for the resistivity $\eta_{\rm nc}$ and the bootstrap current $j_{\rm bs}$ (Ref. 22), respectively. The total toroidal current is related to the poloidal field as usual through Ampère's law: $j_\zeta \equiv j_{\rm tor} = (c/4\pi)(1/r)(\partial/\partial r)(rB_\theta)$. The radial electric field $\langle E_r \rangle$ is determined by averaging the radial momentum balance relation

$$E_r = \hat{\mathbf{e}}_r \cdot \left[-\frac{\mathbf{v} \times \mathbf{B}}{c} + \frac{1}{en}\nabla p_i \right]. \tag{2}$$

The poloidal flow velocity (toroidal flows are included in CUTIE but are not significant for COMPASS which had no external momentum inputs) satisfies

$$\frac{\partial \langle u_\theta \rangle}{\partial t} = -\nu_{\rm nc}[\langle u_\theta \rangle - u_{\rm nc}] + \langle L_\theta \rangle, \tag{3}$$

where $\nu_{\rm nc}$ is the flow-damping rate and $u_{\rm nc}$ is the poloidal velocity in neoclassical theory.[22] The poloidal acceleration due to turbulence is given by

$$\langle L_\theta \rangle = -\frac{1}{r}\frac{\partial}{\partial r}(r\langle \delta u_\theta \delta u_r \rangle) - \frac{2\langle \delta u_\theta \delta u_r \rangle}{r} + \hat{\mathbf{e}}_\theta \cdot \frac{\langle \delta \mathbf{j} \times \delta \mathbf{B} \rangle}{m_i n}. \tag{4}$$

These equations and the particle and energy transport equations of a similar structure[19,20] determine the self-consistent evolution of relevant profiles. The structure of turbulent fluxes shows that rapid local variation of the turbulent fluctuations causes rapid local evolution of the zonal flows and dynamo currents crucial to self-organization. Thus, if the turbulent fluctuations occur at some typical frequency $\omega_{\rm turb} \simeq \omega_{*e,i}$, the quadratic dependence of the fluxes (which are merely flux surface averages) imply both a 0 frequency (in reality on the inverse transport time-scale) and a rapidly oscillating component in the mean gradients. The latter is responsible for rapid "profile-turbulence" interactions and the corrugations seen in the current density and zonal flow profiles. Thus, contrary to common approximations, there is no genuine "time-scale separation" between the turbulence and mean-profile evolution in global simulations.

CUTIE is a "large eddy simulation" code which needs some mechanism to prevent energy transferred through linear and nonlinear "direct cascade" of enstrophy to subgrid scales from spuriously reappearing at long wavelengths (such spurious effects are known as "aliasing"). Indeed, shear Alfvén waves and flows provide an extremely efficient mechanism to transfer energy (and more particularly enstrophy) to subion gyroradius scales, where kinetic/collisional effects can be expected to randomize phases efficiently and prevent energy from returning coherently to longer wavelengths. The net effect of such dynamical "phase-mixing"[19] is turbulent diffusion in both real and wave-number/frequency spaces. The cutoff at high wavenumbers (subgrid) is provided by a turbulent effective diffusivity which is a function of the local (flux-averaged) enstrophy. On the other hand, the strongly advective character of the fluxes at scales larger than the ion gyroradius is modeled explicitly.

B. Plasma edge

It is known that in COMPASS-D, shaping effects and X-point geometry played a role in the dynamics of H-mode. However, the simulation of the region between closed and open field lines [scrape-off-layer (SOL)] is a well known problem in numerical simulations of plasmas with a separatrix such as COMPASS-D. In CUTIE simulations the X-point geometry is accounted for by an introduction of simple particle and energy sink in the region $r/a > 0.95$. This sink is complemented by a particle source in the confinement region $(r/a < 0.95)$ as will be described below. Such a combination of sink and source gives rise, in effect, to the formation of sharp density gradient at the edge, similar to that in the experiment. This density gradient is located somewhat inside of

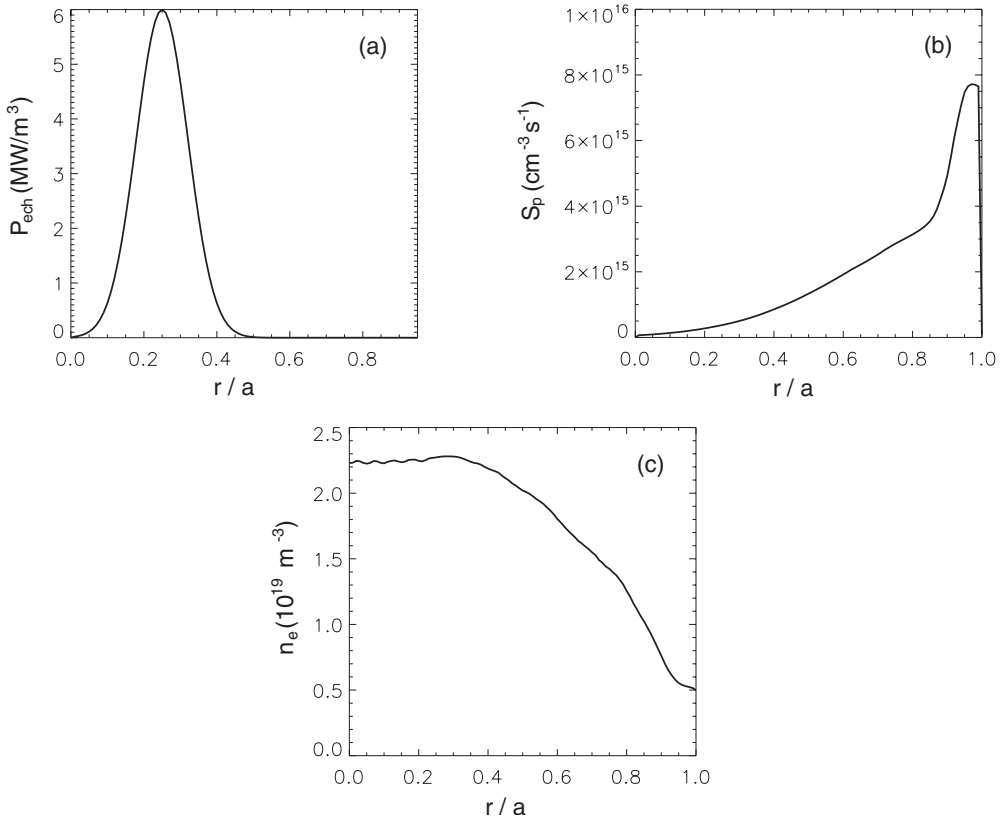

FIG. 2. (a) ECH source-profile, (b) particle source, and (c) electron density profile at 260 ms, in L-mode used in CUTIE simulations.

the "edge" of the sink and this is where the transport barrier develops.

Thus the region occupied in the solution domain by the plasma extends radially from $r/a=0$ to $r/a=0.95$. The "vacuum/SOL edge region" outside this has very low (fixed) density, temperature, and current. All fluctuating quantities are set to 0 at the "wall" located at $r/a=1$. No boundary conditions are set at $r/a=0.95$ but edge sources and sinks are prescribed to "fuel" the discharge.

Setting up the boundary condition for density at $r/a=0.95$ is the only effect of artificial sink. The region representing the SOL $r/a>0.95$ is therefore not modeled in physically accurate detail in our CUTIE simulations and we do not refer to any phenomena in this region.

IV. CUTIE SIMULATIONS

We now present the results obtained in our simulations of the COMPASS-D conditions described in Sec. I. The simulation conditions are as follows: plasma current $I_p=242$ kA and toroidal field $B_{\mathrm{tor}}=2.07$ T. This corresponds to an edge $q_{\mathrm{cyl}}=4.3$. The ECH power input (i.e., power absorbed in the plasma as estimated in the experiments) is 340 kW. The line-averaged density is controlled by feedback using a source of the general form $S_p=S(r/a)[\bar{n}_{\mathrm{target}}-\bar{n}]/\tau_r$, whenever the calculated line-average density $\bar{n}$ is less than the "target" density $\bar{n}_{\mathrm{target}}$. Here $S(r)$ is a fixed profile peaking at the edge and τ_r is a fuelling time set to 100 μs. The power deposition and particle source profiles used in the simulation have the radial structure shown in Figs. 2(a) and 2(b). In addition to the auxiliary power, the Ohmic power is calculated using standard formulae; it contributes only about 30 kW (about 15% of P_{ECH}).

This whole simulation covered the time interval approximately 50 ms (from 245 to 295 ms according to an arbitrary initial time). During this simulation, the plasma current, toroidal field, shape, and ECRH power were kept constant. The only control parameter which was varied in the model was the plasma density using the density feedback (i.e., $\bar{n}_{\mathrm{target}}$) as described above. Three distinct phases are observed during this simulation which are described below.

A. L-mode phase (245–262 ms)

The simulation is started by adjusting the line-averaged density to the required level of target density ($\bar{n}_{\mathrm{target}}=1.8\times10^{19}$ m^{-3}). During this period the turbulence and the profiles are fully developed and initial transients decay away. The plasma characteristics suggest that it is in a quasisteady, "L-modelike" state during this phase. In Fig. 2(c) we show the electron density profile at 260 ms toward the end of this phase. It clearly does not exhibit any "edge pedestal-like" structures. The same is true of both electron and ion temperature profiles (not shown) at this time.

B. ELM-free H-mode phase (262–272 ms)

At 262 ms an attempt was made to induce a L-H transition by increasing the line-averaged density holding the auxiliary input power constant. The target line-averaged density is set to $\bar{n}_{\mathrm{target}}=5.3\times10^{19}$ m^{-3}. The plasma line-averaged

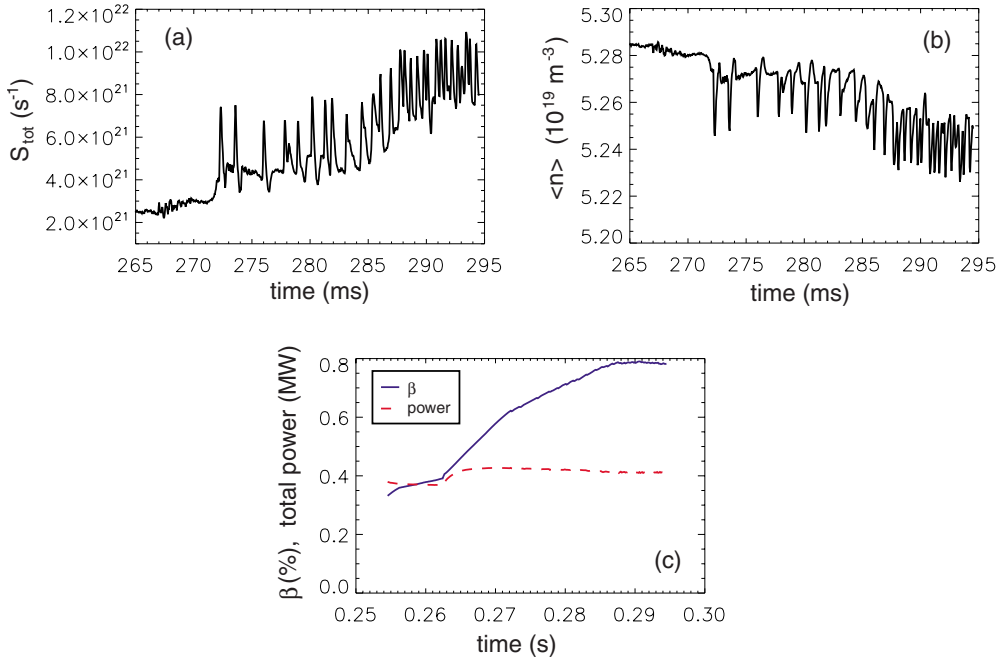

FIG. 3. (Color online) (a) Particle source rate S_{tot} wave-form, (b) plasma line-averaged density $\bar{n}_e$ wave-form during H-mode (265–295 ms); note ordinate scale in b. The initial density rise due to source is not shown. (c) The total power input (MW) and the toroidal $\beta(\%)$ from 255 to 295 ms.

density $\bar{n}$ responds to this increased particle fuelling by rising to just below $\bar{n}_{target}$ in about 200 μs (of the order of τ_r). The particle source rises sharply during this phase, nearly tripling the total number of plasma electrons injected per second (and ions, since the source is quasineutral).

The response of the simulated discharge to this imposed particle source change is shown in Fig. 3. In Figs. 3(a) and 3(b) the particle source and line-average density wave-forms are shown from about 265 ms, around 3 ms after the enhanced fuelling rate is introduced. We have suppressed the initial (transient) phase (from 262 to 265 ms) when the new target density increases both the source and the line-averaged density. The figures show the behavior of the line-averaged density and source *after* the former starts fluctuating close to (but slightly below) the target value (5.3×10^{19} m^{-1}). Remembering that this is a "feed-back control," it is clear that the source rises sharply whenever an abrupt increase in particle transport to the edge occurs. Thus, this waveform has similar behavior to D_α traces measured in tokamaks. In particular, the sharp increases in fuelling rate are qualitatively similar to ELMs. It is noteworthy that the injection of particles starts at 262 ms and the plasma initially remains rather "quiescent" with an ELM-free period lasting up to 272 ms with line-average density $\leq 5.3\times10^{19}$ m^{-3}. In Fig. 3(c) we show the plasma toroidal $\beta(\%)$ and the total power $P_{tot}=P_{Ohmic}+P_{ec}$ as functions of time from 255 to 295 ms (namely, over the whole simulation). The power is seen to rise slightly when the target density is increased at 262 ms due to increased Ohmic heating at constant current. The toroidal beta increases linearly relatively rapidly until the first ELM starts at 272 ms. It continues to increase at a slower rate during the ELMy H-mode, until around 285 ms it saturates when the ELM frequency rises. It is clear from the power and beta wave-forms that the energy confinement has increased after 262 ms.

We show the particle source-profile (in units of particles injected per cm^3/s) at 270 ms in Fig. 4(a) and the corresponding density profile [Fig. 4(b)]. The source rate is reduced relative to L-mode and the density profile is hollow. The central ion temperature (not shown) falls from around 420 eV (before the source switch-on) to 260 eV at 270 ms. The ion temperature is also found to be hollow, resembling the density profile at 270 ms and has a relatively steep gradient at the edge unlike the L-mode profile. It must be remembered that in this simulation, electrons are heated by ECH and through Ohmic heating, whereas the ions are heated solely through the classical, collisional electron-ion energy exchange, which depends strongly upon the electron density and temperature.

It is instructive to comment on the response of the plasma enstrophy averaged over the whole plasma and the measure of magnetic fluctuation energy which are available. A study of these turbulence diagnostics shows that both quantities rise fivefold immediately following the fuelling relative to preinjection levels. The enstrophy per unit volume, a measure of electrostatic turbulence, starts to decrease soon after reaching a peak at 264 ms, whereas the magnetic fluctuation energy saturates at a higher level. Detailed investigations show that the turbulence (both electrostatic and magnetic components) in the core region increases substantially after source switch-on but the turbulence in the edge decreases significantly.

During this period, the stored energies in both electrons and ions rise steadily [as clearly shown by Fig. 3(c)], even though P_{ecrh} is maintained constant (at 340 kW). Since the total current is also fixed, the rise in the electron density

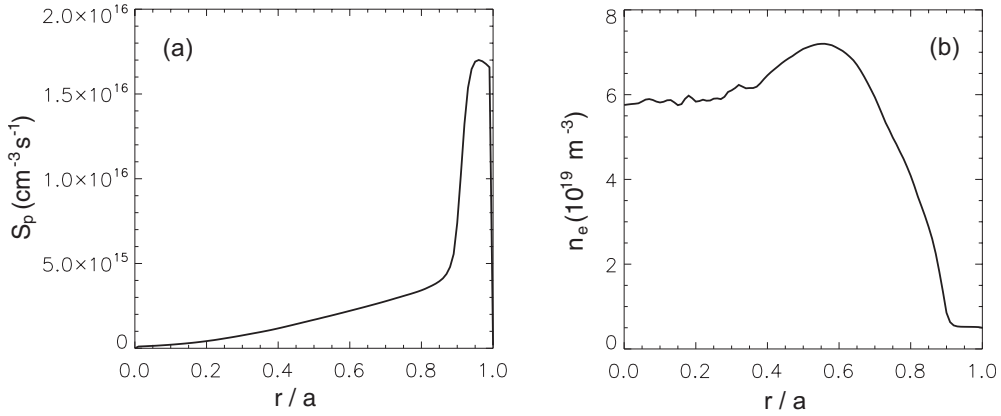

FIG. 4. (a) Particle source-profile and (b) n_e profile at 270 ms. Note change of scale relative to Figs. 2(b) and 2(c).

results in a corresponding fall in the electron temperature which increases the plasma resistivity. This increases the Ohmic heating rate, from 50 kW to about 80 kW, ≃25% of the auxiliary ECH power input to the plasma [also shown in Fig. 3(c)]. The reduction in the edge turbulence is also responsible for the "continuous" transition of the system (according to the present CUTIE model) from an L-mode into an ELM-free H-mode at around 270 ms.

In Figs. 5(a) we present the wave-form of the poloidal $E\times B$ flow $V_{\rm pol}=-cE_r/B_{\rm tor}$ at $r/a=0.9$ from 255 to 278 ms (thus including L-mode, ELM-free H, and initial ELMy H-mode phases). Thus, Fig. 5(a) shows that the flow and the radial electric field shear are small in the L-phase. After the L-H transition at 262 ms the flow increases monotonically up to 20 km/s in the electron diamagnetic direction (positive) at 272 ms. When the first ELM-like event occurs at this time, the flow velocity is reversed to −10 km/s (in the ion diamagnetic direction). After the ELM, the velocity recovers to

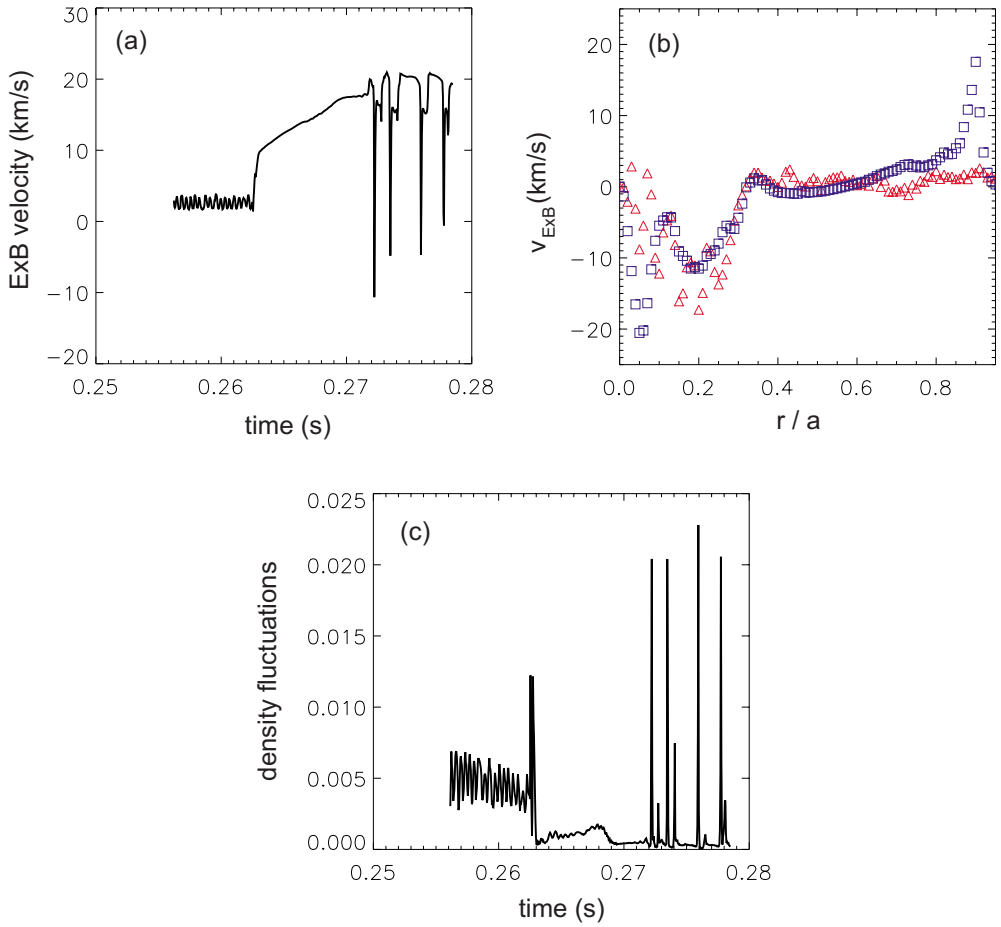

FIG. 5. (Color online) (a) Radial electric field E_r at $r/a=0.9$ shown in terms of the poloidal $E\times B$ velocity from 255 to 278 ms. (b) Poloidal $V^{E\times B}$ flow profiles ($0\le r/a\le 0.95$) during L-mode (260 ms; red triangles) and in H-mode (270 ms; blue squares). (c) The density fluctuation wave-form at $r/a=0.9$ shown during the same time period.

$\simeq$20 km/s in two successive steps ($-10 \rightarrow 15 \rightarrow 20$ km/s). Thereafter this wave-form is repeated with an inter-ELM period of 1–2 ms. The profiles of $V_{\text{pol}}=-cE_r/B_{\text{tor}}$ [presented in Fig. 5(b)] at 260 and 270 ms show that strong shear layers develop in the ELM-free H-mode, both at the edge and in the deep core (this is related to the $q=1$ mode rational surface and the turbulence in its vicinity).

Figure 5(c) shows the density fluctuation wave-form at $r/a=0.9$ (dn/n_0 normalized to the central value) increasing sharply when the target density is raised at 262 ms but then rapidly falls to a much lower value lower than in L-mode during the "ELM-free" phase (262 to 272 ms). The "spikes" due to ELM-like events are much higher, nearly ten times the amplitude during the quiescent phase. Clearly the density fluctuation wave-form is anticorrelated with the spikes in the flow at the same location and time. The profile of the magnetic fluctuations at 270 ms (not shown) has been compared with corresponding L-mode profiles and shows that while the core fluctuations are not seriously altered in magnitude, the edge magnetic turbulence is greatly reduced, possibly by an order of magnitude when the line-averaged density is increased from 1.8×10^{19} to $\simeq5.0\times10^{19}$ m^{-3}.

C. ELMy H-mode phase (272–295 ms)

The first ELM occurs spontaneously at 272 ms confirming that the plasma was previously in an ELM-free state and with good confinement (indicated by steadily rising stored energy at constant power) for about 10 ms following the onset of refueling. There is an obvious and strong correlation between the spikes in particle source rate and the inverted $\bar{n}_e$ spikes shown in Fig. 3(b). While the source rate increases by more than 50% at each ELM, the line-average density variation is much smaller, showing that the loss is primarily an edge phenomenon. Around 285 ms, we see that the ELM frequency increases [seen in both Figs. 3(a) and 3(b)]. The line-average density wave-form (with a falling trend) reflects the steady loss of particle confinement and has a lower level even though the source rate has increased on average toward the end of the period. The particle source rate, on the other hand exhibits a rising trend [see Fig. 3(a)], reflecting poor particle confinement as the ELM frequency rises. It is noteworthy that these dynamical changes seen in the trends from the computed wave-forms are "evolutionary" and do not arise from any change in external inputs ($\bar{n}_{\text{target}}$, current, field, and auxiliary power).

As stated earlier, the dynamical evolution of the plasma from this point on is not driven by any externally imposed change in the power or particle sources. The simulations show [exemplified in Fig. 3(c), for example] that the plasma spontaneously evolves into a state with strong edge localized activity (ELMs). It is clearly seen that between 272 and 287 ms, there are sharp "crashes" with a spacing on the average of about 1.5 ms, getting more frequent (though not significantly less in amplitude) toward 285 ms when the frequency roughly doubled. We note that these crash events have the qualitative characteristics of strong ELMs.

In Figs. 6(a) and 6(b) we present the typical behavior of ELMs, taking as an example the first ELM (at approximately 272 ms). Figure 6(a) shows the density profile at 272.14 ms (just before the crash) and at 272.18 ms (at the "peak" of the crash amplitude) in the region $0.75\leq r/a\leq0.95$. It should be mentioned that the plasma edge in these simulations is defined to be at $r/a=0.95$. It is clear that the ELM has significantly lowered the "pedestal" density of around 3×10^{19} m^{-3} to about 2.5 and consequently decreased the density gradient. To conserve particles, the density is found to be increased for $r/a>0.87$. It is interesting to consider the effect of the ELM on the radial electric field E_r. In Fig. 6(b) we present the plots of the calculated $V_{\text{pol}}=-cE_r/B_{\text{tor}}$ for the same region and instants. It is evident that the strong shear layer is almost reversed. The simulations reveal, however that the electric field recovers its pre-ELM profile in about 100 μs. Figures 6(c) and 6(d) show the effect of the ELM on the electron and ion temperature profiles, pedestals, and gradients. The electron temperature gradient is relevant both to the total pressure gradient which drives the MHD instabilities and to the edge bootstrap current density gradients. The ITG is linked to the radial electric field and its shear and to lesser extent to the driving pressure gradient (ions are colder than electrons). These gradients play complex interacting roles in the dynamics of the ELM instabilities.

In Fig. 7(a) the radial profiles of the rms density fluctuations in the edge region are shown for five time points spaced by 40 μs. The very first curve (black-solid line) shows the density fluctuation profile immediately pre-ELM. It is clear that the fluctuation levels (note that they are normalized not to the local density but to the central density at that instant) are very low for $r/a>0.85$. Forty microseconds into the ELM (red-dotted line) shows that the fluctuations have increased ten-fold to about 1.2% at $r/a=0.87$ where the steepest density gradient occurs (pre-ELM) in Fig. 7(a). At 80 μs into the ELM (green dashed line) we see that the fluctuation nearly doubles to reach 2.5% at $r/a=0.88$. It has also become much broader ranging from $r/a=0.85$ to 0.95. In the next 40 μs, the turbulence "collapses" equally rapidly (blue dotted-dash curve). Finally, around 160 μs from the start, we see that the density fluctuation level is almost identical with the initial state (cyan dashed-dotted-dot curve). This pattern is repeated (although never strictly periodically) at all other ELM-like crashes in the edge region and can therefore be regarded as describing the generic dynamical behavior.

In Figs. 8(a) and 8(b) the density fluctuation contours are presented in a poloidal plane. Some features of the turbulence can be clearly seen in these plots (note that the scale in color is linear, so that low amplitude features are not visible). It is clear that the strongest perturbations in density occur in the edge region and are associated with strong ballooning (outboard side fluctuations are clearly much stronger) and associated with relatively high poloidal mode numbers. The radial and poloidal wave-number dependence of the ion temperature and density fluctuations corresponding to Fig. 8(b) are shown in Figs. 9(a) and 9(b). We define the relative density fluctuation spectral function depending upon the mode number $m, r/a, t$ according to the relation, $dn/n_0=\{\sum_{\nu=1}^{\nu_{\max}}[dn/n]_{m,\nu}^2(r/a,t)\}^{1/2}$ (where the summation is over ν, the toroidal mode number in the Fourier component $[dn/n]_{m,\nu}(r/a,t)$ and $n_{\max}$ is the maximum toroidal harmonic

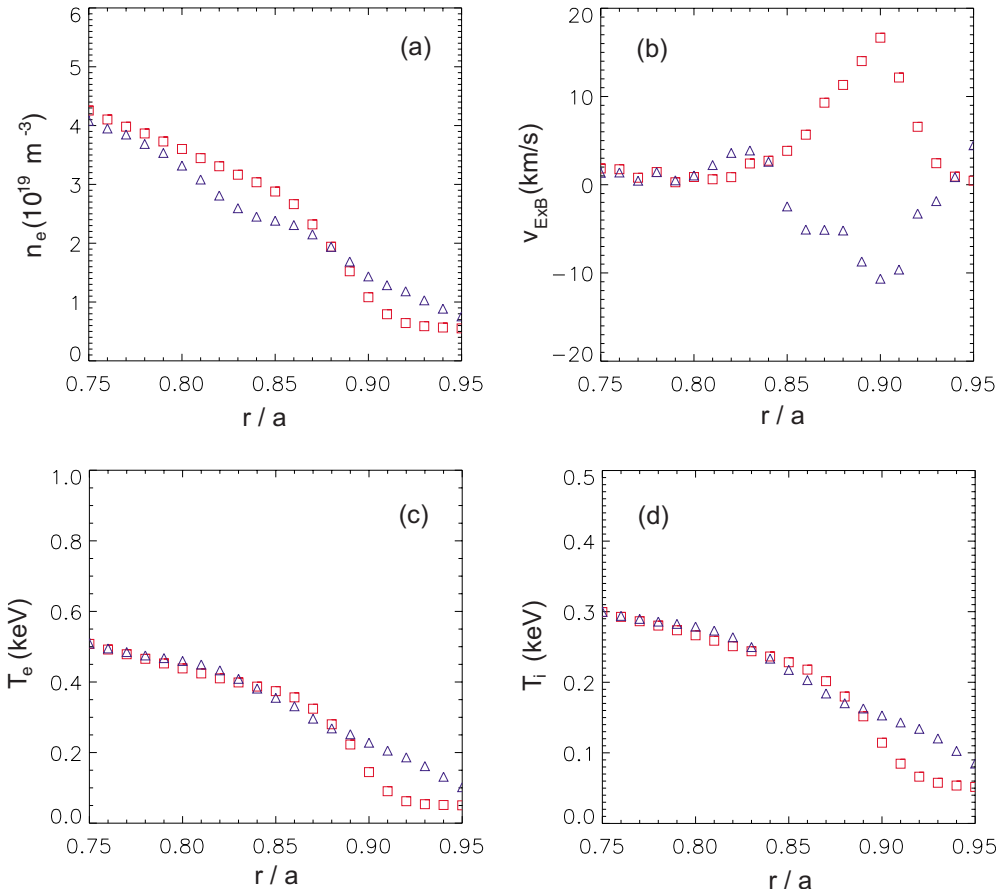

FIG. 6. (Color online) H-mode profiles: (a) n_e, (b) $V^{E\times B}$, (c) T_e and (d) T_i, just before (red squares) and 40 μs later (blue triangles), during ELM at 272 ms.

used in the simulation). The ion temperature fluctuations are defined similarly. The edge modes correspond to the range $m=10-20$; $n=2-5$. The rotation of these modes is complex and not simply associated with the poloidal flow directions.

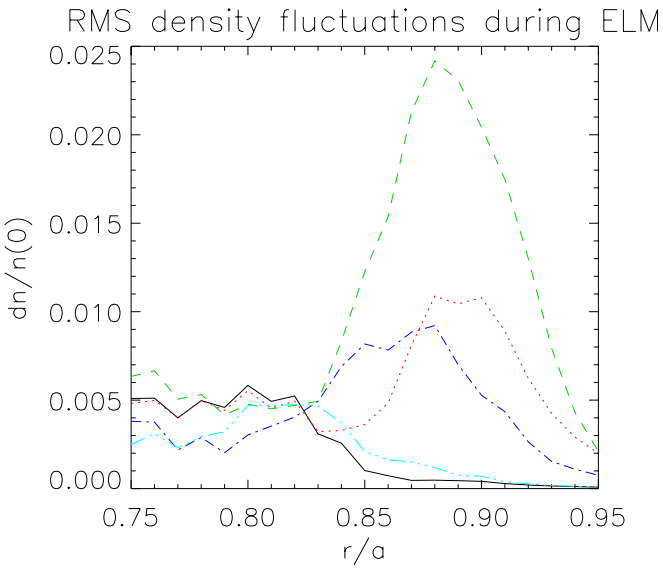

FIG. 7. (Color online) RMS density fluctuation profiles $\delta n/n(0)$ during ELM (272.14 ms) at 40 μs intervals: black-solid (0), red-dotted (40), green dash (80), blue dotted-dash (120), and cyan dashed-dotted-dot (160).

As the ELMy H-mode phase progresses the ELM frequency increases [see Figs. 3(a) and 3(b)]. The ELM character during the high ELM frequency phase is however still quite similar to the first ELM after the ELM-free H-mode phase. This is shown in Figs. 10(a) and 10(b) where ion temperature fluctuations during the late ELMy phase are displayed. While in the core, an $m=1$ mode dominates and the edge perturbation has $m\simeq 15,16$ and is ballooning strongly. This mode reaches peak amplitude in about 40 μs. When the simulation is run even longer the plasma seems to approach the "continuous ELMing" phase with the ELM frequency increasing to 1 kHz. Detailed analysis however shows that electric field in the ETB is still present between the high frequency ELMs and thus the back-transition to L-mode has not been reached yet. It is observed that the increase of ELM frequency is correlated with the decrease of amplitude of radial electric field at the edge. This could indicate that the increase of ELM frequency is a consequence of destabilization of ballooning modes responsible for ELMs due to reduced flow shear. The transition from ELMy H-mode to L-mode is the subject of on-going systematic investigations.

V. DISCUSSION AND CONCLUSIONS

This work demonstrates that a two-fluid electromagnetic plasma model in which profiles are allowed to evolve can show a remarkable resemblance to L-H transitions observed

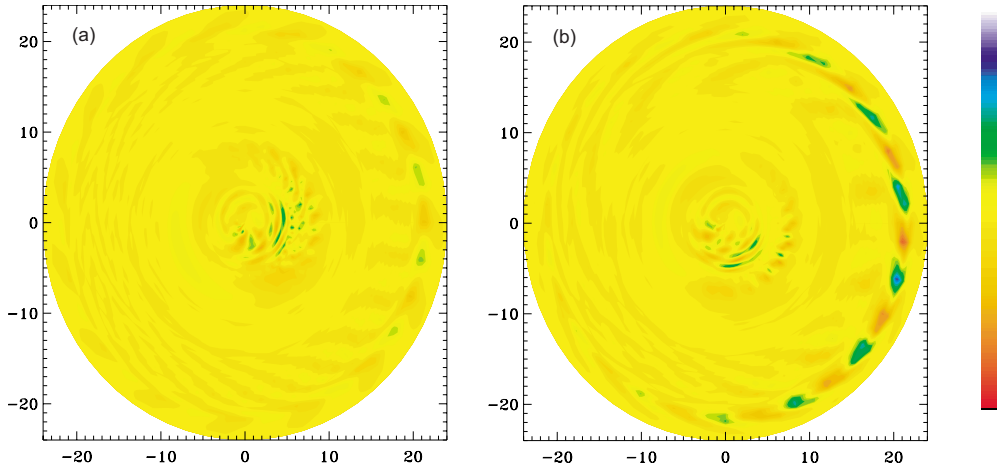

FIG. 8. (Color online) (a) Pre-ELM (272.14 ms) dn/n_0 contours and (b) contours at ELM-crash (272.18 ms).

in COMPASS-D. A key element of our model is the introduction of particle and energy sinks at the edge. This, combined with the particle source in the confinement zone, creates a sharp density gradient and this could be responsible for the L-H transition. In simulations the L-H transition is induced by increased edge particle source at constant heating power from core electron heating using ECH. This creates a density and temperature pedestal in the edge region; the edge turbulence is then suppressed and a state approximating an ELM-free H-mode is obtained. The stored energies in both species rise steadily and the particle confinement is enhanced. The radial electric field (as represented by the poloidal $E\times B$ flow) in the edge region acquires a strongly sheared, jetlike structure. Our simulation supports the standard paradigm of L-H transition: $E\times B$ shear (see, for example, Refs. 4–6 and 23) causes the quench of the L-mode turbulence which appears to be a mix of drift-Alfvén and fluid ITG modes. The new element in our simulation is that the $E\times B$ shear is driven by the density gradient controlled by a combination of the particle source inside separatrix and sink outside the separatrix.

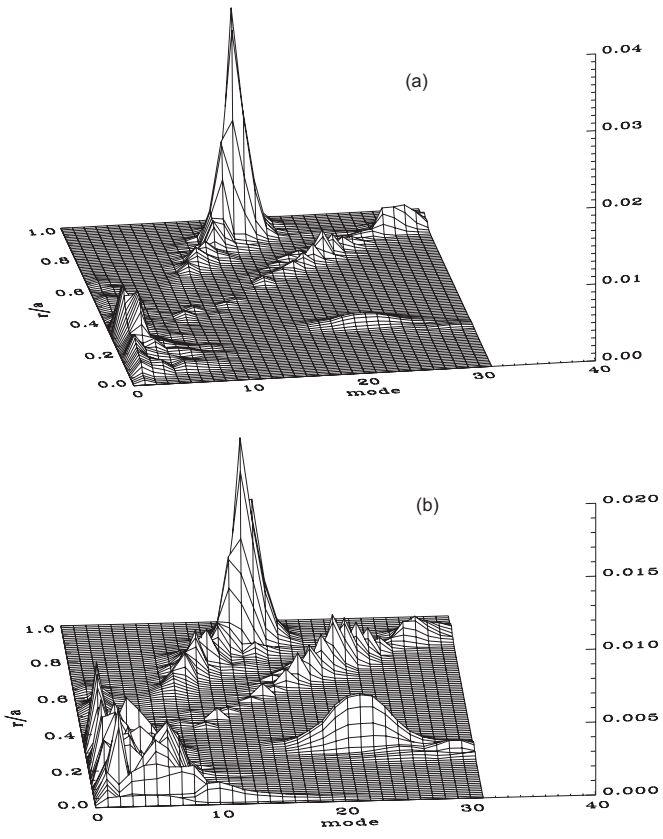

FIG. 9. Spectra (r/a vs m) at ELM-crash (272.18 ms): (a) dT_i/T_{i0} and (b) dn/n_0.

A question might be raised whether the transition to improved confinement is not simply an accumulation effect caused by increased particle source and reduced particle transport due to the favorable parametric density dependence (e.g., a reduction in $\eta_i = d\ln T_i/d\ln n$ or the Alfvén velocity/growth time-scale $\propto n^{-1/2}$). This of course could be a contributing factor. However in our case, the formation of the ETB as manifested by increased radial electric field and the existence of ELMs are clear features of the standard H-mode regime.

It might seem contradictory that the L-H transition is induced by an increased particle source while in experiments adding gas usually degrades the H-mode. In our simulation, the L-H transition is related to the density threshold of H-mode transition where it is well known that at constant power a minimum density is required for the transition. Our simulations are also consistent with the observations in COMPASS-D where continuous outboard gas puffing did not readily create an H-mode in Ohmic plasmas. However when the gas valve, after reaching certain plasma density, was switched off the H-mode was obtained. This points to the importance of profiling of particle source and sink which is responsible for the sharp density gradient across the separatrix.

Increased density gradient at the separatrix is a central element in our model of L-H transition. This model is independent (quantitatively) of the details of physical processes in the SOL. The location of X-point can obviously change flow patterns outside the separatrix and thus affect the density gradient at the last closed flux surface. These additional effects are not captured in our model and thus we cannot

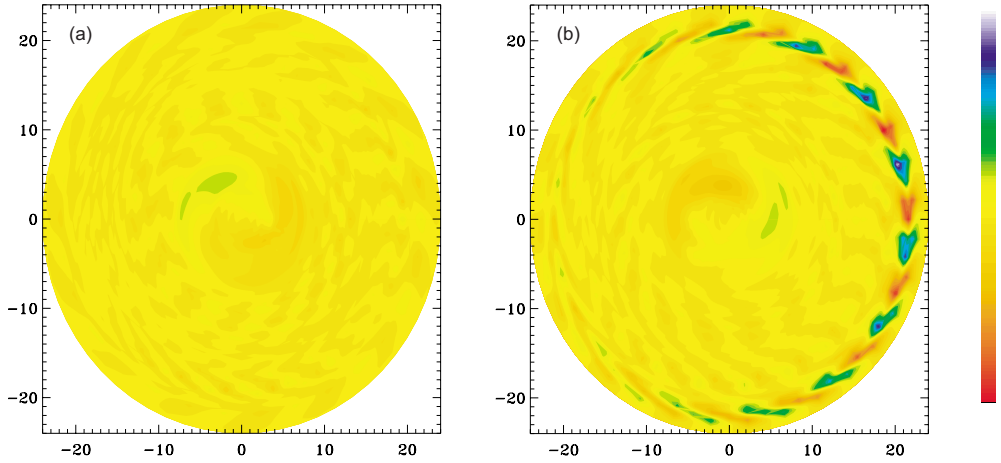

FIG. 10. (Color online) (a) Pre-ELM (291.46 ms) dT_i/Ti_0 contours and (b) contours at ELM-crash (291.50 ms).

predict quantitatively the dependence of density thresholds on the direction of ion grad-B drift relative to the X-point. Note however that the fact that limiter H-modes also exist supports our model.

Concerning the causality question, in our simulation the chain of events starts with the increased particle source. This, combined with SOL sink, leads to the sharper density gradient which in turn increases the $E \times B$ shear. After the turbulence is quenched, the density gradient increases further. In the simulation the transition and the rate of change of $E \times B$ shear evolve simultaneously, as is well known in experiments.

CUTIE simulations also show that the ELM-free H-mode is later spontaneously interrupted by MHD phenomena resembling ELMs. With no external changes, the edge stability is lost and one gets strongly ballooning MHD crashes, initially in 1–2 ms intervals. During these events the edge density fluctuations sharply increase, edge radial (sheared) electric field and density and temperature gradients are reduced. The whole event lasts about 100 μs and plasma recovers relatively fast so that the overall confinement is not degraded. Indeed, the stored energies continue to increase through many such crashes. The simulations also suggest that the system is not in a stationary state; as time progresses the ELM frequency increases. The nature of modes underlying the ELMs is unlikely to be simple. The ballooning character of the perturbation indicates that it is a pressure-driven instability but the contribution of kinklike "peeling modes" driven by the edge bootstrap current density cannot be ruled out. The question might be asked why ELMs appear as repetitive bursts and not like continuous modes with constant amplitude. The reason for this is a strongly nonlinear character of the loop responsible for ELMs dynamics: pressure gradient, mode amplitude, plasma transport caused by the mode, and reduced pressure gradient. Such a system does not necessarily reach a steady state as has been demonstrated in a nonlinear dynamical model of sawteeth and ELMs due to one of the authors in Ref. 7

The code allows neoclassical transport coefficients to be included everywhere. It turns out that the effective turbulent transport coefficients which are self-consistently calculated by coevolution of the mean profiles and the fluctuations subject to the externally prescribed sources are almost everywhere much larger. The effects of trapped particles on the turbulence are not taken into account in the code (hence trapped particle modes of instability are not included in the simulations) nor are kinetic effects such as Landau damping and subion gyroradius physics. These limitations (particularly those associated with geometry and trapped particle effects on fluctuations) suggest that the CUTIE model is truly "minimalist" in including only mesoscale physics.

Our focus in this work has throughout been on obtaining qualitative insight into the dynamic description of phenomena on resistive (i.e., rather long) time-scales. The net result of our simplified model is that it is possible to study electromagnetic relaxation and transition phenomena on experimentally relevant "macro-" time-scales and the whole tokamak volume (including the sawtoothing region) not generally accessible to most kinetic global/flux-tube codes Refs. 24–27 A price one pays for such breadth is that one can (at best) expect only qualitatively correct results. It is therefore not a little surprising that CUTIE seems to be able to capture many detailed features of the experiments in spite of the stated limitations of the model. This would appear to suggest that the dynamics underlying ETBs and ELMs is fundamentally robust and not qualitatively dependent upon the physics omitted in our minimalist model. The simulations also suggest that a proper understanding of the phenomena we have investigated cannot be obtained without including mesoscale physics correctly and describing profile-turbulence interactions in which the sources are given but the gradients in the profiles and the transport matrix are outcomes of the calculation, not held fixed *a priori*.

We discuss briefly the relationship of our work to earlier ones we have cited. Clearly, the "shear-flow paradigm" as elaborated in the references[4–6,23] plays an essential role in our simulations. Furthermore, we see that many features of ELM dynamics discussed in simpler nonlinear models due to Carreras *et al.*[4] and by one of the authors and a co-worker in Ref. 7 are reflected, albeit in a much more complicated system of nonlinear partial differential equations driven by sources and sinks in our results. In essence, our work comes

closest to the simulations of Huysmans *et al.*[8] These authors also find the pressure-driven ballooning instability to be the cause of the phenomena. While the JOREK code is a very sophisticated, fully three-dimensional simulation tool, capable of modeling the open field-line regions as well as a fully toroidal plasma equilibrium (these features lie outside the scope of CUTIE, as already discussed), transport and two-fluid effects included in CUTIE are not present. The two approaches are clearly complementary. The work of Rogers *et al.*[2] and Kleva and Guzdar[3] invoke the resistive ballooning modes and the drift-Alfvén branches. Although there are many points of contact between these works and the present one, they seem not to be sufficient to account for the phenomena in COMPASS-D discussed here.

As far as we are aware, the present simulations are the first ones to suggest a possible physical explanation of L to H transitions and associated relaxation phenomena relating to ETBs based on two-fluid electromagnetic turbulence modified by drift effects at a given constant power when the plasma density is increased, at least in the case of COMPASS-D (an electron-heated device). They certainly point to the importance of the particle and energy sources in the formation, maintenance, and dynamics of ETBs. It is likely that more detailed edge modeling and inclusion of the full toroidal equilibrium geometry (including X-point regions) and shaping effects will enable more quantitatively accurate results to be obtained, which can be compared in detail with quantitative measurements. The present simulations suggest that fairly robust two-fluid generalizations of MHD will suffice to get some general insights into L-H transitions and ELM phenomena.

ACKNOWLEDGMENTS

This work was funded by the United Kingdom Engineering and Physical Sciences Research Council under Grant No. EP/G003955 and the European Communities under the contract of Association between EURATOM and CCFE. The views and opinions expressed herein do not necessarily reflect those of the European Commission. The authors thank Tim Hender and Colin Roach for useful discussions and suggestions. We also thank the referee and the editor for stimulating and thoughtful comments and useful suggestions for improving the paper.

APPENDIX: CUTIE EQUATIONS

We reproduce the equations used in CUTIE to make this paper self-contained (more details are available in the references cited, in particular in Refs. 18 and 19)

$$\frac{\partial n}{\partial t} + \nabla \cdot (n\mathbf{v}) = S_p, \tag{A1}$$

$$m_i n \frac{d\mathbf{v}}{dt} = -\nabla p + \frac{\mathbf{j}\times\mathbf{B}}{c} + \mathbf{F}_{\text{eff}}, \tag{A2}$$

$$\frac{3}{2}\frac{dp_{e,i}}{dt} + p_{e,i}\nabla\cdot\mathbf{v}_{e,i} = -\nabla\cdot\mathbf{q}_{e,i} + P_{e,i}, \tag{A3}$$

$$\mathbf{E} + \frac{\mathbf{v}_e\times\mathbf{B}}{c} = -\frac{\nabla p_e}{en} + \mathbf{R}_e, \tag{A4}$$

$$\nabla\times\mathbf{B} = \frac{4\pi\mathbf{j}}{c}. \tag{A5}$$

The following definitions apply: $(m_i+m_e)\mathbf{v}=m_i\mathbf{v}_i+m_e\mathbf{v}_e$ and $\mathbf{B}=\nabla\psi\times\mathbf{b}_t+B_0\mathbf{b}_t$, where $\mathbf{b}_t$ is the unit vector in the "toroidal" direction. The electric field $\mathbf{E}=-(1/c)(\partial\psi/\partial t)\mathbf{b}_t-\nabla\phi$, and the plasma pressure, $p=p_e+p_i=n(T_e+T_i)$. The external particle source is represented by S_p while the effective force on the plasma is taken to be $\mathbf{F}_{\text{eff}}$. The electron-ion friction force is $\mathbf{R}_e$ while $\mathbf{q}_{e,i}$ are the heat-flux vectors. In CUTIE the "periodic cylinder" approximation to tokamak geometry is used; the polar coordinate θ represents the "poloidal" angle and $\zeta=z/R$ is the "toroidal" angle. The flux surfaces are labeled by the cylindrical radial coordinate r. This approximation is relevant when the "inverse aspect ratio" $\epsilon=a/R$ of the device is small. The representation of the electric field in terms of the two potentials ϕ,ψ given above also follows from "tokamak ordering;" in this, the magnetic field fluctuations *parallel* to the equilibrium field are neglected compared to the fluctuations in the r,θ (or "poloidal") plane. Following nondimensional dependent variables and decompositions are applied; $f(r,\theta,\zeta,t)=f_0(r,t)+f^*(r,\theta,\zeta,t)$ where the (position space) "fluctuation amplitudes" f^* are not necessarily small, but do depend on both angular variables and are expanded in double Fourier series

$$f^* = \sum_{m=-\infty}^{\infty}\sum_{n=-\infty}^{\infty}\hat{f}_{m,n}(r,t)\exp(im\theta+in\zeta). \tag{A6}$$

By definition, the "mean" $f_0(r,t)$ represents the $m=n=0$ Fourier component of the variable $f(r,\theta,\zeta,t)$ and consequently $\hat{f}_{0,0}\equiv 0$. The Fourier coefficients satisfy the reality condition $\hat{f}_{m,n}=\bar{\hat{f}}_{-m,-n}$, where the over-bar denotes complex conjugation. The electromagnetic fields are described in terms of two potentials ϕ and ψ. These are *fluctuating* parts (thus, $\delta\mathbf{E}=-\nabla\phi-(1/c)(\partial\psi/\partial t)\mathbf{e}_\zeta$). The corresponding mean quantities are denoted by $\Phi_0(r,t),\Psi_0(r,t)$.

The following dimensional parameters are employed: the "Alfvén velocity" $\bar{V}_A^2=B_0^2/4\pi m_i n(0,t)$; the "sound velocity" $\bar{V}_{\text{th}}^2=[T_e(0,t)+T_i(0,t)]/m_i$; "ion gyrofrequency" $\omega_{ci}=eB_0/m_ic$; "effective gyroradius" $\rho_s=\bar{V}_{\text{th}}/\omega_{ci}$; "plasma beta" $\beta=(\bar{V}_{\text{th}}/\bar{V}_A)^2$. In addition, we introduce the potential vorticity [with dimensions, $(1/T)$], $\Theta=\nabla\cdot[n_0(r,t)/n_0(0,t)\nabla_\perp(cphi/B_0)]$. We also define the nondimensional fluctuations ϕ^*,ψ^*,Θ^*: $\frac{c\phi}{B_0}=\bar{V}_{\text{th}}\rho_s\phi^*$; $\frac{\psi}{B_0}=\rho_s\beta^{1/2}\psi^*$ $\Theta=\frac{\bar{V}_{\text{th}}}{\rho_s}\Theta^*$; $\Theta^*=\rho_s^2\nabla\cdot\left[\frac{n_0(r,t)}{N^*}\nabla_\perp\phi^*\right]$ and $n^*=\delta n_e/N^*$; $\lambda_{i,e}^*=\delta T_{i,e}/T^*$; $\xi^*=n_0(r,t)\delta v_\parallel/\bar{\xi}$, where $N^*=n_e(0,t)$, $T^*=T_e(0,t)+T_i(0,t)$ and $\bar{\xi}=N^*\bar{V}_{\text{th}}$. Note that we nondimensionalize only the *dependent* variables. The system is thus described completely by these variables and the corresponding mean quantities which are conveniently chosen to be $n_0(r,t),T_{e0}(r,t),T_{i0}(r,t),v_{\theta 0}(r,t),v_{\zeta 0}(r,t),E_{r0}(r,t),B_{\theta 0}(r,t)$. Several different advection velocities occur in the theory. By definition, $E_{r0}=-\partial\Phi_0/\partial r$. The velocity $\mathbf{u}_0=-cE_{r0}/B\mathbf{e}_\theta$

$+\mathbf{b}_0 v_{\|0}$ represents the equilibrium "MHD" flow of the plasma (ions), while $\mathbf{u}_{e0}$ represents the corresponding electron flow $\mathbf{u}_{e0}=-cE_{r0}/B\mathbf{e}_\theta+\mathbf{b}_0(v_{\|0}-j_{\|0}/en_0)$. The ion fluid flow (i.e., MHD flow + diamagnetic flow) is given by $\mathbf{v}_0=\mathbf{u}_0+(c/en_0B)(\partial p_{i0}/\partial r)\mathbf{e}_\theta$. We also have the relation $\Theta_0=(1/r)(\partial/\partial r)[rn_0(r,t)/N^*(c/B_0)(\partial\Phi_0/\partial r)]$. Finally, $\mathbf{v}_{e0}=-[(cE_{r0}/B)+(c/en_0B)(\partial p_{e0}/\partial r)]\mathbf{e}_\theta$ is the total electron *poloidal flow* composed of the electron $\mathbf{E}\times\mathbf{B}$ equilibrium flow and the electron diamagnetic flow. In the following, $\nabla_\|\equiv\mathbf{b}_0\cdot\nabla=(1/qR)[(\partial/\partial\theta)+q(\partial/\partial\zeta)]$ (i.e., the gradient in the direction of the *unperturbed field*). The nonlinear terms account for the exact field direction.

The equations of motion governing the spatiotemporal evolution of the electromagnetic fluctuations, with these conventions, are the following:

$$\Theta^*=\rho_s^2\nabla\cdot\left(\frac{n_0}{N^*}\nabla_\perp\phi^*\right), \tag{A7}$$

$$\begin{aligned}\frac{\partial\Theta^*}{\partial t}&+\mathbf{v}_0\cdot\nabla\Theta^*+\bar{V}_A\nabla_\|\rho_s^2\nabla_\perp^2\psi^*\\&=\bar{V}_A\rho_s\frac{1}{r}\frac{\partial\psi^*}{\partial\theta}\frac{4\pi\rho_s}{cB_0}j_0'+\bar{V}_{\rm th}\rho_s\frac{1}{r}\frac{\partial(\psi^*,\rho_s^2\nabla_\perp^2\psi^*)}{\partial(r,\theta)}\\&+\bar{V}_{\rm th}\rho_s\left[\frac{1}{r}\frac{\partial(\Theta^*,\phi^*)}{\partial(r,\theta)}+\left(\frac{N^*T_{i0}}{n_0T^*}\right)\frac{1}{r}\frac{\partial(\Theta^*,n^*)}{\partial(r,\theta)}\right]\\&-\frac{2\bar{V}_{\rm th}\rho_s}{R_0}\left[\frac{\cos\theta}{r}\frac{\partial p^*}{\partial\theta}+\sin\theta\frac{\partial p^*}{\partial r}\right]+\rho_s^2\Theta_0'\frac{1}{r}\frac{\partial\phi^*}{\partial\theta}+\Sigma_\Theta^*,\end{aligned} \tag{A8}$$

$$\begin{aligned}\frac{\partial\psi^*}{\partial t}&+\mathbf{v}_{e0}\cdot\nabla\psi^*+\bar{V}_A\nabla_\|\phi^*\\&=\bar{V}_A\left(\frac{N^*T_{e0}}{n_0T^*}\right)\nabla_\|n^*+\bar{V}_{\rm th}\rho_s\\&\times\left[\frac{1}{r}\frac{\partial(\psi^*,\phi^*)}{\partial(r,\theta)}-\left(\frac{N^*T_{e0}}{n_0T^*}\right)\frac{1}{r}\frac{\partial(\psi^*,n^*)}{\partial(r,\theta)}\right]+\Sigma_\psi^*.\end{aligned} \tag{A9}$$

These are supplemented by the continuity equation for the quasineutral (electron) density, two energy equations, and the ion parallel momentum equation

$$\begin{aligned}\frac{\partial n^*}{\partial t}&+\mathbf{u}_{e0}\cdot\nabla n^*+\bar{V}_A\nabla_\|\rho_s^2\nabla_\perp^2\psi^*+\bar{V}_{\rm th}\nabla_\|\xi^*\\&=\bar{V}_A\rho_s\frac{1}{r}\frac{\partial\psi^*}{\partial\theta}\frac{4\pi\rho_s}{cB_0}j_0'+\bar{V}_{\rm th}\rho_s\frac{1}{r}\frac{\partial(\psi^*,\rho_s^2\nabla_\perp^2\psi^*)}{\partial(r,\theta)}\\&+\bar{V}_{\rm th}\rho_s\frac{1}{r}\frac{\partial(n^*,\phi^*)}{\partial(r,\theta)}+\bar{V}_{\rm th}\rho_s\left(\frac{n_0'}{N^*}\right)\frac{1}{r}\frac{\partial\phi^*}{\partial\theta}\\&-\frac{2\bar{V}_{\rm th}\rho_s}{R_0}\left[\frac{\cos\theta}{r}\frac{\partial p_e^*}{\partial\theta}+\sin\theta\frac{\partial p_e^*}{\partial r}\right]+\Sigma_n^*.\end{aligned} \tag{A10}$$

$$\begin{aligned}\frac{\partial\xi^*}{\partial t}&+\mathbf{u}_0\cdot\nabla\xi^*+\bar{V}_{\rm th}\left(\frac{T_{e0}+T_{i0}}{T^*}\right)\nabla_\|n^*\\&=\left(\frac{n_0v_{\|0}'}{N^*}\right)\rho_s\frac{1}{r}\frac{\partial\phi^*}{\partial\theta}+\bar{V}_{\rm th}\rho_s\frac{1}{r}\frac{\partial(\xi^*,\phi^*)}{\partial(r,\theta)}\\&-\bar{V}_{\rm th}\rho_s\beta^{1/2}\left(\frac{p_0'}{P^*}\right)\frac{1}{r}\frac{\partial\psi^*}{\partial\theta}\\&-\bar{V}_{\rm th}\rho_s\beta^{1/2}\frac{1}{r}\frac{\partial(p^*,\psi^*)}{\partial(r,\theta)}-\bar{V}_{\rm th}\left(\frac{n_0}{N^*}\right)\nabla_\|(\lambda_i^*+\lambda_e^*)+\Sigma_\xi^*.\end{aligned} \tag{A11}$$

$$\begin{aligned}\frac{3}{2}&\left[\frac{\partial\lambda_i^*}{\partial t}+\mathbf{u}_0\cdot\nabla\lambda_i^*\right]+\bar{V}_{\rm th}\left(\frac{N^*T_{i0}}{n_0T^*}\right)\nabla_\|\xi^*\\&=\frac{3}{2}\bar{V}_{\rm th}\rho_s\left[\frac{1}{r}\frac{\partial(\lambda_i^*,\phi^*)}{\partial(r,\theta)}+\left(\frac{T_{i0}'}{T^*}\right)\frac{1}{r}\frac{\partial\phi^*}{\partial\theta}\right]\\&+\left(\frac{T_{i0}}{T^*}\right)\frac{2\bar{V}_{\rm th}\rho_s}{R_0}\left[\frac{\cos\theta}{r}\frac{\partial p_i^*}{\partial\theta}+\sin\theta\frac{\partial p_i^*}{\partial r}\right]\\&+\left(\frac{T_{i0}}{T^*}\right)\frac{2\bar{V}_{\rm th}\rho_s}{R_0}\left[\frac{\cos\theta}{r}\frac{\partial\phi^*}{\partial\theta}+\sin\theta\frac{\partial\phi^*}{\partial r}\right]+\Sigma_{\lambda_i}^*.\end{aligned} \tag{A12}$$

$$\begin{aligned}\frac{3}{2}&\left[\frac{\partial\lambda_e^*}{\partial t}+\mathbf{u}_{e0}\cdot\nabla\lambda_e^*\right]+\bar{V}_{\rm th}\left(\frac{N^*T_{e0}}{n_0T^*}\right)\nabla_\|\xi^*\\&=\frac{3}{2}\bar{V}_{\rm th}\rho_s\left[\frac{1}{r}\frac{\partial(\lambda_e^*,\phi^*)}{\partial(r,\theta)}+\left(\frac{T_{e0}}{T^*}\right)\frac{1}{r}\frac{\partial\phi^*}{\partial\theta}\right]\\&-\left(\frac{N^*T_{e0}}{n_0T^*}\right)\bar{V}_A\nabla_\|\rho_s^2\nabla_\perp^2\psi^*-\left(\frac{T_{e0}}{T^*}\right)\frac{2\bar{V}_{\rm th}\rho_s}{R_0}\\&\times\left[\frac{\cos\theta}{r}\frac{\partial p_e^*}{\partial\theta}+\sin\theta\frac{\partial p_e^*}{\partial r}\right]+\left(\frac{T_{e0}}{T^*}\right)\frac{2\bar{V}_{\rm th}\rho_s}{R_0}\\&\times\left[\frac{\cos\theta}{r}\frac{\partial\phi^*}{\partial\theta}+\sin\theta\frac{\partial\phi^*}{\partial r}\right]+\Sigma_{\lambda_e}^*.\end{aligned} \tag{A13}$$

The fluctuating source terms (the Σ^*s) contain self-consistent turbulent diffusion terms dependent on the local fluctuating potential vorticity and current density. Thus, typically $\Sigma_f^*=\nabla\cdot D_{\rm turb}\nabla f^*$ for the fluctuating quantity f^*. Here, $D_{\rm turb}$ is taken to depend upon $\Theta^*,\rho_s^2\nabla_\perp^2\psi^*$, the highest spatial derivatives of ϕ^*,ψ^* in the system. It is analogous to eddy diffusivity terms familiar from aerodynamics and meteorology. These sinks are needed to provide the "high wave-number cutoff" required to prevent undesirable aliasing effects of Fourier truncations of fluctuations. The above equations are supplemented by the evolution equations governing the "mean potentials" $[\Phi_0(r,t),\Psi_0(r,t)]$ and those relevant to $n^*,\lambda_{e,i}^*$, etc. Let $f_0(r,t)$ be a typical mean (e.g., particle density). The full equations of motion imply that, upon taking the $m=0$, $n=0$ Fourier component (equivalently averaging over an equilibrium flux surface r), this evolves according to

$$\frac{\partial f_0}{\partial t}=-\frac{1}{r}\frac{\partial}{\partial r}[r\Gamma_f(r,t)]+S_f(r,t). \tag{A14}$$

Here, Γ_f represents the *total* flux of the quantity f across the flux surface. In general, this flux is due to transport processes due to collisions which are present even in the absence of turbulence, as well as turbulence-caused fluxes. Thus, one may write generally $\Gamma_f \equiv \Gamma_f^{\text{coll}} + \Gamma_f^{\text{turb}}$. The fluxes Γ_f^{coll} include the so-called "classical" and "neoclassical" terms, which can be advective and/or diffusive and may also involve both f_0 and its radial gradients as well as other fields, such as temperatures, etc. Within the fluid model, turbulent fluxes are mainly advective ones, due essentially to the fluctuating $\mathbf{E}\times\mathbf{B}$ drifts across the flux surfaces. These take the general form

$$\Gamma_f^{\text{turb}} = \langle \delta V_r f^* \rangle = \frac{1}{4\pi^2}\int_0^{2\pi}\int_0^{2\pi} \delta V_r(r,\theta,\zeta,t) f^*(r,\theta,\zeta,t) d\theta d\zeta, \quad \text{(A15)}$$

where δV_r is the turbulent radial $(\mathbf{E}\times\mathbf{B})$ velocity fluctuation and f^* is the fluctuating part of f. Note that the average in question is *not* a time-average, but one over the equilibrium flux surface at r. In principle, these turbulent components *can* and do vary rapidly, i.e., on the "fast" turbulent length (in the radial direction) and time-scales. This term is crucial in introducing local, mesoscale "corrugations" in $f_0(r,t)$. In the special case of electrons, the large *parallel* heat transport implies, in the presence of turbulence, an effective *radial* transport (i.e., $\langle \mathbf{q}_{\|e} \rangle$ can make a substantial contribution to the heat-flux across equilibrium surfaces). The source S_f is also the effective surface averaged source derived from the full equations of motion.

Equilibrium density and temperature values (typically 5×10^{19} m^{-3} and 100 eV, respectively) are prescribed at the "wall" $r/a=1.0$. The total plasma current is prescribed; this amounts to specifying $B_\theta(r/a=1.0)$. At the origin (i.e., magnetic axis), equilibrium density and temperature (and potential) profiles must satisfy zero gradient conditions. All fluctuating potentials and quantities are set to 0 at the magnetic axis and at the wall (not at the plasma edge at r/a=0.95). Initial profiles are arbitrarily prescribed, although the transients settle quickly if reasonable initial ones are given. For the semi-implicit, pseudospectral solution method, the reader is referred to the works cited. The results depend only upon sources and after a sufficiently long time become independent of initial data.

[1] R. Aymar, P. Barabaschi, and Y. Shimomura, Plasma Phys. Controlled Fusion **44**, 519 (2002).
[2] B. N. Rogers, J. F. Drake, and A. Zeiler, Phys. Rev. Lett. **81**, 4396 (1998).
[3] R. G. Kleva and P. N. Guzdar, Phys. Plasmas **13**, 072509 (2006).
[4] B. A. Carreras, P. H. Diamond, Y.-M. Liang, V. Lebedev, and D. Newman, Plasma Phys. Controlled Fusion **36**, A93 (1994).
[5] K. Itoh, S.-I. Itoh, and A. Fukuyama, *Transport and Structural Formation in Plasmas* (IOP, Bristol, 1999), p. 222 *et seq*.
[6] A. Yoshizawa, S.-I. Itoh, and K. Itoh, *Plasma and Fluid Turbulence* (IOP, Bristol, 2003), p. 331 *et seq*.
[7] A. Thyagaraja, F. A. Haas, and D. J. Harvey, Phys. Plasmas **6**, 2380 (1999).
[8] G. T. A. Huysmans, S. Pamela, E. van der Plas, and P. Ramet, Plasma Phys. Controlled Fusion **51**, 124012 (2009).
[9] J. W. Connor, A. Kirk, AIP Conf. Proc. **1013**, 174 (2008).
[10] S. J. Fielding, M. Valovič, P. G. Carolan, D. A. Gates, C. Hunt, P. Leahy, A.W. Morris, and the COMPASS-D Physics and ECRH Teams, Plasma Phys. Controlled Fusion **40**, 731 (1998).
[11] M. Valovič, S. J. Fielding, B. Lloyd, S. J. Manhood, A. W. Morris, T. Pinfold, K. Stammers, C. D. Warwick, and the COMPASS-D and ECRH Teams, in*Proceedings of the 26th EPS Conf. on Contr. Fusion and Plasma Phys.*, edited by B. Schweer, G. Van Oost, and E. Vietzke, Maastricht, 1999 (European Physical Society, Nieuwegein, 1999), Vol. ECA 23J, p. 149.
[12] S. J. Fielding, R. J. Buttery, A. R. Field, P. B. Jones, H. Meyer, M. Valovič, H. R. Wilson, and the COMPASS-D and ECRH Teams, *Proceedings of the 28th EPS Conf. on Contr. Fusion and Plasma Phys.*, edited by C. Silva, C. Varandas, and D. Campbell, Madeira, 2001 (European Physical Society, Funchal, 2001), Vol. ECA 25A, p. 1825.
[13] S. J. Fielding, A. R. Field, M. Valovič, H. R. Wilson, P. G. Carolan, J. W. Connor, N. J. Conway, J. Dowling, B. Lloyd, A. W. Morris, and the COMPASS-D Physics and ECRH Teams, Plasma Phys. Controlled Fusion **42**, A191 (2000).
[14] M. Valovič, P. G. Carolan, A. R. Field, S. J. Fielding, P. B. Jones, B. Lloyd, H. Meyer, M. Price, V. Shevchenko, K. Stammers, M. J. Walsh, S. You, and the COMPASS-D Physics and ECRH Teams, Plasma Phys. Controlled Fusion **44**, A175 (2002).
[15] A. R. Field, P. G. Carolan, N. J. Conway, G. F. Counsell, G. Cunningham, P. Helander, H. Meyer, D. Taylor, M. R. Tournianski, M. J. Walsh, and the MAST team, Plasma Phys. Controlled Fusion **46**, 981 (2004).
[16] P. Gohil, L. R. Baylor, T. C. Jernigan, K. H. Burrell, and T. N. Carlstrom, Phys. Rev. Lett. **86**, 644 (2001).
[17] M. Valovič, K. Axon, L. Garzotti, S. Saarelma, A. Thyagaraja, R. Akers, C. Gurl, A. Kirk, B. Lloyd, G. P. Maddison, A. W. Morris, A. Patel, S. Shibaev, R. Scannell, D. Taylor, M. J. Walsh, and the MAST Team, Nucl. Fusion **48**, 075006 (2008).
[18] A. Thyagaraja, Plasma Phys. Controlled Fusion **42**, B255 (2000).
[19] A. Thyagaraja, P. J. Knight, and N. Loureiro, Eur. J. Mech. B/Fluids **23**, 475 (2004).
[20] M. R. de Baar, A. Thyagaraja, G. M. D. Hogeweij, P. J. Knight, and E. Min, Phys. Rev. Lett. **94**, 035002 (2005).
[21] A. Thyagaraja, P. J. Knight, M. R. de Baar, G. M. D. Hogeweij, and E. Min, Phys. Plasmas **12**, 090907 (2005).
[22] R. D. Hazeltine and J. D. Meiss, *Plasma Confinement* (Addison-Wesley, New York, 1992).
[23] P. H. Diamond, S.-I. Itoh, K. Itoh, and T. S. Hahm, Plasma Phys. Controlled Fusion **47**, R-35 (2005).
[24] T. Dannert and F. Jenko, Phys. Plasmas **12**, 072309 (2005).
[25] W. Deng and Z. Lin, Phys. Plasmas **16**, 102503 (2009).
[26] J. Candy, C. Holland, R. E. Waltz, M. R. Fahey, and E. Belli, Phys. Plasmas **16**, 060704 (2009).
[27] W. Dorland, F. Jenko, M. Kotschenreuther, and B. N. Rogers, Phys. Rev. Lett. **85**, 5579 (2000).